V International Conference on Computational Methods for Coupled Problems in Science and Engineering
COUPLED PROBLEMS 2013
S. Idelsohn, M. Papadrakakis and B. Schrefler (Eds)

ADAPTIVE FINITE ELEMENT LIMIT ANALYSIS INCORPORATING STEADY STATE PORE PRESSURES

SCOTT W. SLOAN, ANDREI V. LYAMIN AND KRISTIAN KRABBENHØFT

ARC Centre of Excellence for Geotechnical Science and Engineering (CGSE)
The University of Newcastle
NSW 2308, Callaghan, Australia
e-mail: scott.sloan@newcastle.edu.au
web page: http://www.cgse.edu.au

Key words: Finite Element, Limit Analysis, Pore Pressures, Coupled Problems.

Abstract. This paper describes an adaptive method for incorporating the pore pressures associated with steady-state seepage in finite element limit analysis. The formulation can model both general seepage conditions, and locating the phreatic surface in unconfined flow presents no special difficulty [1]. Since the proposed method employs the same mesh for the upper analysis, the lower-bound analysis and the pore pressure computation, there is no need to import and interpolate the pore-pressures from another grid (or program). This is a significant practical advantage and leads to an efficient solution process.

In the iterative solution method, a Hessian(curvature)-based error estimator is applied to the pore pressure field to generate a mesh which gives accurate pore pressures. Simultaneously, a variant of the 'bounds gap' error estimator of [2],[3] is employed to identify a separate mesh which gives accurate upper and lower bounds on the limit load. By combining these two strategies, a hybrid refinement strategy is developed which minimises both the bounds gap and the error in the computed pore pressures.

1 INTRODUCTION

Finite element limit analysis has become an important tool for predicting the load capacity of geostructures such as foundations, retaining walls, tunnels and slopes. These methods are based on discrete formulations of the limit theorems [4],[5] and lead to large sparse optimisation problems which can be solved very efficiently. In this paper, the pore pressures are incorporated using the upper bound procedures described in [6],[7], the lower bound procedure described in [8], and the algorithms described in [1]. After briefly describing the discrete bound formulations, we outline a variant of the scheme proposed in [2],[3] which measures the contribution of each element to the 'bounds gap'. This 'bounds gap' estimator relies on using an identical discretization for the upper and lower bound analyses, and provides a very effective means for refining the mesh to give accurate solutions. Next, we describe a procedure for computing steady-state pore pressures. This method uses the same mesh as the bound procedures, and permits the effect of pore pressures on the limit load to be modelled accurately. Finally, the formulation is used to study the stability of a slope with a weak layer.

2 UPPER BOUND FORMULATION

The upper bound formulation follows that described in [6], with the enhancements described in [7] to model velocity discontinuities. In an upper bound calculation we search for a velocity distribution $\mathbf{u} = \{u_x, u_y\}^{\mathrm{T}}$ which satisfies compatibility, the flow rule, the velocity boundary conditions $\mathbf{w}$ on the surface area A_w, and minimises the internal power dissipation less the rate of work done by the fixed external loads. The latter quantity can be written as

$$\dot{W} = \int_V \boldsymbol{\sigma}^{\mathrm{T}} \dot{\boldsymbol{\varepsilon}}^p \,\mathrm{d}V - \int_{A_t} \mathbf{t}^{\mathrm{T}} \mathbf{u} \,\mathrm{d}A - \int_V \mathbf{g}^{\mathrm{T}} \mathbf{u} \,\mathrm{d}V \tag{1}$$

where $\boldsymbol{\sigma} = \{\sigma_{xx}, \sigma_{yy}, \tau_{xy}\}^{\mathrm{T}}$ is a vector of stresses, $\dot{\boldsymbol{\varepsilon}}^p = \{\dot{\varepsilon}^p_{xx}, \dot{\varepsilon}^p_{yy}, \gamma^p_{xy}\}^{\mathrm{T}}$ is a vector of plastic strain rates, $\mathbf{t}$ are fixed surface tractions acting on the area A_t, $\mathbf{g}$ are fixed body forces, and V is the volume of the body. The first integral on the right hand side of (1) corresponds to the plastic dissipation P_{int}. Once the velocity field which minimizes $\dot{W}$ has been found, the optimized value of $\dot{W}$ can be equated to the power expended by the external loads

$$P_{ext} = \int_{A_q} \mathbf{q}^{\mathrm{T}} \mathbf{u} \,\mathrm{d}A + \int_V \mathbf{h}^{\mathrm{T}} \mathbf{u} \,\mathrm{d}V \tag{2}$$

to find an upper bound on the unknown surface tractions $\mathbf{q}$ (acting over the area A_q) or the unknown body forces $\mathbf{h}$ (acting over the volume V). Note that the latter are included to permit optimisation of body forces, such as the unit weight, which is very useful in modelling slopes, excavations, and tunnels. The 2D continuum element used in the upper bound formulation is shown in Fig. 1. Over each triangle, the unknown velocities $\mathbf{u}$ are assumed to vary linearly while the unknown element stresses $\boldsymbol{\sigma}^e$ are assumed to be constant. Although it is possible to develop upper bound formulations without the stresses $\boldsymbol{\sigma}^e$, they are included because they permit general types of yield surfaces to be modelled. Moreover, they also enable a simple error estimate to be formulated which measures the 'bounds gap' contribution of each element directly.

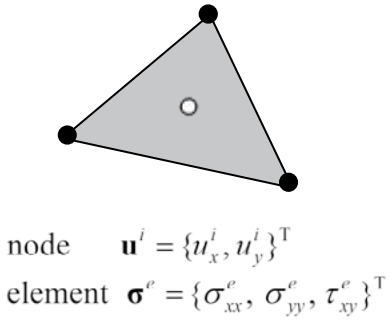

Figure 1: Upper bound element

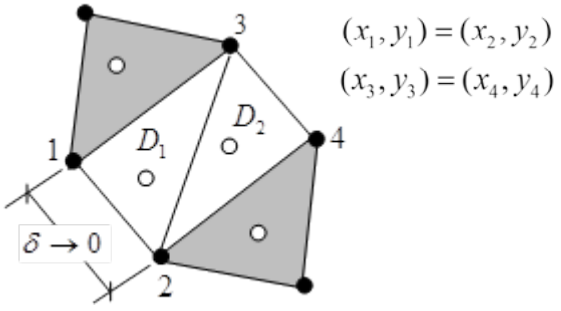

Figure 2: Velocity discontinuity

Following the approach proposed in [7], kinematically admissible velocity discontinuities are modelled by using a patch of zero-thickness continuum upper bound elements, as shown in Fig. 2. The elements D_1 and D_2 are standard upper bound elements, except that two of the nodal co-ordinates are set to be identical, and the flow rule equations are multiplied by the

element areas. This strategy ensures the velocity jumps across the discontinuity are kinematically admissible [7] , leads to an efficient formulation in 2D and 3D, and does not require special algorithms when computing the 'bounds gap' error estimator [1]. The discrete formulation of the upper bound theorem leads to a large, sparse, nonlinear optimisation problem where $\dot{W}$ in equation (1) is the quantity that is minimised over the field of unknowns $(\boldsymbol{\sigma},\mathbf{u})$. After assembling the objective function coefficients and constraints for a 2D mesh, this optimisation problem can be expressed as

$$
\begin{array}{lllll}
\text{Minimise} & \boldsymbol{\sigma}^{\mathrm{T}}\overline{\mathbf{B}}\,\mathbf{u} & -\mathbf{c}^{\mathrm{T}}\mathbf{u} & \text{power dissipation - rate of work done by fixed external forces} \\
\text{Subject to} & \overline{\mathbf{B}}^{e}\,\mathbf{u}^{e} & = \dot{\alpha}^{e}\,\nabla f(\boldsymbol{\sigma}^{e}) & \text{flow rule conditions for each element } e \\
 & \dot{\alpha}^{e} & \geq 0 & \text{plastic multiplier times } A^{e} \text{ for each element } e \\
 & \dot{\alpha}^{e} f(\boldsymbol{\sigma}^{e}) & = 0 & \text{consistency condition for each element } e \\
 & \mathbf{A}\,\mathbf{u} & = \mathbf{b} & \text{velocity boundary conditions, load constraints} \\
 & f(\boldsymbol{\sigma}^{e}) & \leq \mathbf{0} & \text{yield condition for each element } e
\end{array}
\tag{3}
$$

where $\boldsymbol{\sigma}$ is a global vector of unknown element stresses, $\mathbf{u}$ is a global vector of unknown nodal velocities, $\overline{\mathbf{B}}^{e}$ is the element compatibility matrix multiplied by the element area, $\overline{\mathbf{B}} = \sum \overline{\mathbf{B}}^{e}$ is a global compatibility matrix, $\boldsymbol{\sigma}^{\mathrm{T}}\,\overline{\mathbf{B}}\,\mathbf{u}$ is the power dissipated by plastic shearing in the continuum and discontinuities, $\mathbf{c}^{\mathrm{T}}\mathbf{u}$ is the rate of work done by fixed tractions and body forces, $\dot{\alpha}^{e}$ is the plastic multiplier times the area for element e, $f(\boldsymbol{\sigma}^{e})$ is the yield function for element e, $\mathbf{A}$ is a matrix of equality constraint coefficients, and $\mathbf{b}$ is a known vector of coefficients. Rather than solve the primal problem (3) directly, it is convenient to consider its dual as discussed in [7]. For 2D Tresca and Mohr-Coulomb yield criteria, which are widely used in geomechanics, the dual optimisation problem can be solved very efficiently using second order cone programming.

3 LOWER BOUND FORMULATION

The discrete lower bound formulation [8] seeks to find a statically admissible stress field $\boldsymbol{\sigma} = \{\sigma_{xx}, \sigma_{yy}, \tau_{xy}\}^{\mathrm{T}}$ which satisfies equilibrium throughout V, balances the prescribed tractions $\mathbf{t}$ on A_t, nowhere violates the yield criterion f so that $f(\boldsymbol{\sigma}) \leq 0$, and maximises the collapse load

$$
Q = \int_{A_q} Q_1(\mathbf{q})\,\mathrm{d}A + \int_{V} Q_2(\mathbf{h})\,\mathrm{d}V \tag{4}
$$

where the functions Q_1 and Q_2 depend on the case at hand. In a footing bearing capacity problem, for example, $Q_2 = 0$ and we wish to maximise the load carried by the tractions normal to a boundary edge, q_n, so that $Q_1 = q_n$. In contrast, for a slope or excavation stability we frequently wish to maximise a dimensionless stability parameter which is a function of the unit weight γ so that $Q_1 = 0$ and $Q_2 = \gamma$. The 2D continuum element used in the lower bound formulation is shown in Fig. 3. Over each triangle, the unknown stresses $\boldsymbol{\sigma}$ are assumed to vary linearly while the unknown element body forces $\mathbf{h}^{e}$ are assumed to be constant.

Following the approach proposed in [9], stress discontinuities are modelled by using a patch of zero-thickness continuum lower bound elements, as shown in Fig. 4. The elements D_1 and D_2 are standard lower bound elements, except that pairs of the nodal co-ordinates are set to be identical (as in the modelling of the velocity discontinuities described in the previous section). To ensure that the normal and shear stresses are continuous everywhere along the discontinuity, so that the solution is statically admissible, the standard equilibrium equations are multiplied by the element areas. This type of formulation is again efficient in both 2D and 3D and is particularly convenient when computing the 'bounds gap' error estimator [1].

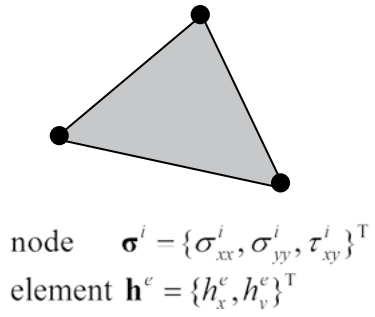

Figure 3: Lower bound element

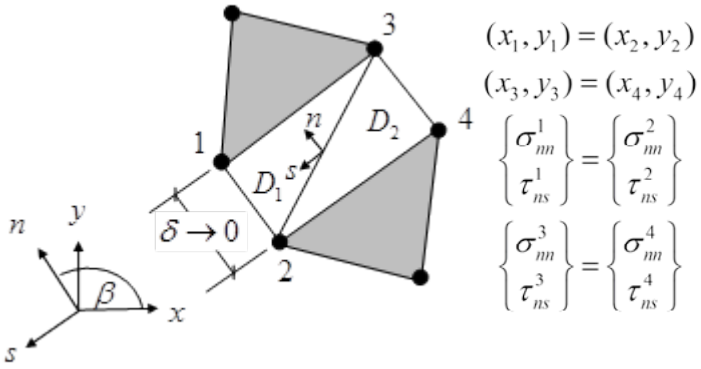

Figure 4: Stress discontinuity

After assembling the objective function coefficients and constraints for a mesh, the load carried by the unknown stresses and body forces, denoted by $\mathbf{c}_1^{\mathrm{T}}\boldsymbol{\sigma}$ and $\mathbf{c}_2^{\mathrm{T}}\mathbf{h}$ respectively, can be maximised by solving the following nonlinear optimisation problem

$$\begin{array}{lrcl} \text{maximise} & \mathbf{c}_1^{\mathrm{T}}\boldsymbol{\sigma} + \mathbf{c}_2^{\mathrm{T}}\mathbf{h} & & \text{collapse load or body force} \\ \text{subject to} & \mathbf{A}_{11}\boldsymbol{\sigma} + \mathbf{A}_{12}\mathbf{h} & = \mathbf{b}_1 & \text{continuum equilibrium} \\ & \mathbf{A}_2\boldsymbol{\sigma} & = \mathbf{b}_2 & \text{discontinuity equilibrium, stress boundary conditions} \\ & f(\boldsymbol{\sigma}^i) & \le \mathbf{0} & \text{yield conditions for each node } i \end{array} \tag{5}$$

where $\mathbf{c}_1$, $\mathbf{c}_2$, $\mathbf{b}_1$, and $\mathbf{b}_2$ are vectors of constants, $\mathbf{A}_{11}$, $\mathbf{A}_{12}$ and $\mathbf{A}_2$ are matrices of constants, f is the nonlinear yield criterion, $\boldsymbol{\sigma}^i$ is a local vector of Cartesian stresses at node i, $\boldsymbol{\sigma}$ is a global vector of unknown Cartesian stresses, and $\mathbf{h}$ is a global vector of unknown body forces acting on each element. As discussed in [10],[11], second order cone programming algorithms have proved to be very efficient for solving (5) when 2D Tresca and Mohr-Coulomb criteria are used.

4 ADAPTIVE MESH REFINEMENT USING BOUNDS GAP MEASURE

To develop an exact measure of the contribution of each element to the bounds gap, we consider the case where identical meshes are used for the upper and lower bound analyses. From the principle of virtual equilibrium, the total plastic dissipation for an upper bound analysis can be written as

$$\int_V \boldsymbol{\sigma}_{UB}^{\mathrm{T}} \dot{\boldsymbol{\varepsilon}}^p \, \mathrm{d}V = \int_{A_q} \mathbf{q}_{UB}^{\mathrm{T}} \mathbf{u} \, \mathrm{d}A + \int_V \mathbf{h}_{UB}^{\mathrm{T}} \mathbf{u} \, \mathrm{d}V + \int_{A_t} \mathbf{t}^{\mathrm{T}} \mathbf{u} \, \mathrm{d}A + \int_V \mathbf{g}^{\mathrm{T}} \mathbf{u} \, \mathrm{d}V \tag{6}$$

where the subscript *UB* denotes upper bounds for the unknown stresses, surface tractions and body forces. Since the velocities $\mathbf{u}$ and plastic strain rates $\dot{\boldsymbol{\varepsilon}}^p$ are kinematically admissible throughout the domain, the principle of virtual equilibrium can be invoked again to give

$$\int_V \boldsymbol{\sigma}_{LB}^{\mathrm{T}} \dot{\boldsymbol{\varepsilon}}^p \, \mathrm{d}V = \int_{A_q} \mathbf{q}_{LB}^{\mathrm{T}} \mathbf{u} \, \mathrm{d}A + \int_V \mathbf{h}_{LB}^{\mathrm{T}} \mathbf{u} \, \mathrm{d}V + \int_{A_t} \mathbf{t}^{\mathrm{T}} \mathbf{u} \, \mathrm{d}A + \int_V \mathbf{g}^{\mathrm{T}} \mathbf{u} \, \mathrm{d}V \tag{7}$$

where $\boldsymbol{\sigma}_{LB}$, $\mathbf{q}_{LB}$ and $\mathbf{h}_{LB}$ are the statically admissible lower bound stresses, tractions, and body forces respectively. Subtracting (7) from (6), the 'dissipation gap' for the mesh, Δ, can be expressed as

$$\Delta = \int_V (\boldsymbol{\sigma}_{UB} - \boldsymbol{\sigma}_{LB})^{\mathrm{T}} \dot{\boldsymbol{\varepsilon}}^p \, \mathrm{d}V = \int_{A_q} (\mathbf{q}_{UB} - \mathbf{q}_{LB})^{\mathrm{T}} \mathbf{u} \, \mathrm{d}A + \int_V (\mathbf{h}_{UB} - \mathbf{h}_{LB})^{\mathrm{T}} \mathbf{u} \, \mathrm{d}V$$

Assuming proportional loading, with the upper and lower bound load multipliers $(\lambda_{UB}, \lambda_{LB})$ defined so that $\mathbf{q}_{UB} = \lambda_{UB}^q \mathbf{q}$, $\mathbf{q}_{LB} = \lambda_{LB}^q \mathbf{q}$, $\mathbf{h}_{UB} = \lambda_{UB}^h \mathbf{h}$ and $\mathbf{h}_{LB} = \lambda_{LB}^h \mathbf{h}$, the equation above becomes

$$\Delta = \int_V (\boldsymbol{\sigma}_{UB} - \boldsymbol{\sigma}_{LB})^{\mathrm{T}} \dot{\boldsymbol{\varepsilon}}^p \, \mathrm{d}V = (\lambda_{UB}^q - \lambda_{LB}^q) \int_{A_q} \mathbf{q}^{\mathrm{T}} \mathbf{u} \, \mathrm{d}A + (\lambda_{UB}^h - \lambda_{LB}^h) \int_V \mathbf{h}^{\mathrm{T}} \mathbf{u} \, \mathrm{d}V \tag{8}$$

In practical calculations, it is usual to optimise either the tractions or the body forces. For cases where the tractions and body forces are optimised simultaneously, the multipliers must be linked (typically through a relation of the form $\lambda^q = \beta \lambda^h$, with β being a prescribed constant). Equation (8) shows that the dissipation gap gives an exact measure of the gap between the upper and lower bounds for a mesh. The contribution of each element to the 'bounds gap', Δ^e, can thus be computed using the expression

$$\Delta^e = \int_{V^e} (\boldsymbol{\sigma}_{UB}^e - \boldsymbol{\sigma}_{LB}^e)^{\mathrm{T}} (\dot{\boldsymbol{\varepsilon}}^p)^e \, \mathrm{d}V = (\boldsymbol{\sigma}_{UB}^e - \boldsymbol{\sigma}_{LB}^e)^{\mathrm{T}} \overline{\mathbf{B}}_e \, \mathbf{u}^e \tag{9}$$

where $\overline{\mathbf{B}}_e$ is the standard compatibility matrix times the element volume and

$$\Delta = \sum_{elements} \Delta^e$$

Since the quantities defined by equation (9) are always positive [12], their values can be used to govern an adaptive mesh refinement process, with each new element size being chosen to be inversely proportional to the magnitude of Δ^e. For each discontinuity element, the bounds gap contribution can be added to the neighbouring continuum element with which it shares the most nodes. A summary of an efficient algorithm for refining the mesh, based on the bounds gap measure Δ^e, can be found in [1].

5 COMPUTING STEADY STATE PORE PRESSURES DUE TO SEEPAGE FLOW

At a point with an elevation head *z*, the steady-state pore pressure *p* is related to the total head *H* by the equation $p = (H - z)\gamma_w$, where γ_w is the unit weight of water. To compute the pore

pressure field, we thus need to solve for the total head which is governed by the well-known equation

$$k(x,y)\nabla^2 H = k(x,y)\frac{\partial^2 H}{\partial x^2} + k(x,y)\frac{\partial^2 H}{\partial y^2} = 0 \tag{10}$$

where $k(x,y)$ is the soil permeability. Using standard variational methods, it can be shown that the solution to (10) is defined by the optimisation problem

$$\text{minimize} \quad \frac{1}{2}\int_V (\nabla H)^{\mathrm{T}} k \nabla H \, \mathrm{d}V \tag{11}$$

subject to appropriate boundary conditions on H. Assuming a linear variation of H over a 3-noded triangular element, the discrete form of this optimisation problem may be written as

$$\begin{aligned} &\text{minimise} \ \frac{1}{2}\mathbf{H}^{\mathrm{T}}\,\mathbf{K}\,\mathbf{H} \\ &\text{subject to} \ \mathbf{A}\mathbf{H} = \mathbf{H}_0 \end{aligned} \tag{12}$$

where $\mathbf{H}$ is a global vector of unknown nodal heads, $\mathbf{H}_0$ is a vector of prescribed values, $\mathbf{A}$ is a matrix specifying the constant head boundary conditions, and $\mathbf{K}$ is a flow matrix defined by

$$\mathbf{K} = \sum_e^E \int_{A^e} \nabla \mathbf{N}_e^{\mathrm{T}} \, k(x,y) \nabla \mathbf{N}_e \, \mathrm{d}A \tag{13}$$

In the equation above, E denotes the number of triangular elements and $\nabla \mathbf{N}^e$ is the gradient of the shape function matrix for element e. The solution to the quadratic programming problem (12) is defined by the equations

$$\mathbf{K}\mathbf{H} = \mathbf{0} \tag{14}$$

with the boundary conditions $\mathbf{A}\mathbf{H} = \mathbf{H}_0$. To avoid the need to transfer the pore pressures from one grid to another, it is convenient to employ the same mesh for the pore pressure and limit analysis calculations. This means, however, that the matrix $\mathbf{A}$ must also contain appropriate terms to ensure that the pore pressure field is continuous across the discontinuities between adjacent triangles [1]. Once (14) has been solved for the nodal heads $\mathbf{H}$, the pore pressures at each node can be found from the relation $\mathbf{p} = (\mathbf{H} - \mathbf{z})\gamma_w$ where $\mathbf{z}$ is a vector of the nodal elevation heads.

If the seepage flow is unconfined, then the phreatic surface must be located and the quadratic optimisation problem (12) is subject to the additional constraint that $\mathbf{p} = (\mathbf{H} - \mathbf{z})\gamma_w \geq 0$. This supplementary condition can be used to compute the pore pressures using the following algorithm described in [1]:

1. Solve (14) to give the nodal heads $\mathbf{H}$.
2. Find the pore pressures at each node from $\mathbf{p} = (\mathbf{H} - \mathbf{z})\gamma_w$.

3. If the change in $\mathbf{H}^{\mathrm{T}}\,\mathbf{K}\,\mathbf{H} \le TOL$, where TOL is a suitably small tolerance, exit with the solution for the pore pressures.
4. For all nodes *i* where the pore pressure $p_i < 0$, adjust the nodal permeability using the relation $\overline{k}_i = s(p)k_i$, where $s(p) = 0.5(1+\tanh(50p))$ is a smoothed step function which lies between 0 and 1.
5. Using (13), recompute $\mathbf{K}$ for each element with the adjusted nodal permeabilities $\overline{k}_i$, then go to step 1.

The smoothed step function in step 4 reduces pore pressure oscillations in the vicinity of the phreatic surface, and the overall process typically requires less than 10 iterations with a stringent convergence tolerance. When computing the contributions to **K** in step 5, the permeability is assumed to vary linearly over each element. This gives a 'weighted' permeability for elements that are bisected by the phreatic surface, and further enhances the rate of convergence of the iteration scheme.

6 UPPER BOUND FORMULATION WITH PORE PRESSURE

To include pore pressure in the upper bound formulation, the effective stress (i.e. the total stress minus the pore pressure) must be used in the yield condition and flow rule equations. The pore pressure field is treated as an auxiliary variable, which varies linearly over each element but is fixed during each limit analysis calculation. Referring to Fig. 1, the upper bound nodal variables are thus $\mathbf{u}^i = \{u_x^i, u_y^i, p\}^{\mathrm{T}}$ while the element effective stresses are $\boldsymbol{\sigma}^e = \{\sigma_{xx}^e - \overline{p},\, \sigma_{yy}^e - \overline{p},\, \tau_{xy}^e\}^{\mathrm{T}}$ where $\overline{p}$ is the pore pressure at the triangle centroid. In addition to these changes, the pore pressures do extra external work so that equation (1) becomes

$$\dot{W} = \int_V \boldsymbol{\sigma}^{\mathrm{T}}\dot{\boldsymbol{\varepsilon}}^p \,\mathrm{d}V - \int_{A_t} \mathbf{t}^{\mathrm{T}}\mathbf{u}\,\mathrm{d}A - \int_V \mathbf{g}^{\mathrm{T}}\mathbf{u}\,\mathrm{d}V - \int_V \nabla p^{\mathrm{T}}\mathbf{u}\,\mathrm{d}V \tag{15}$$

where $\nabla p = \{\partial p/\partial x,\, \partial p/\partial y\}^{\mathrm{T}}$ is the gradient of the pore pressure field. Since the pore pressure is assumed to vary linearly, this gradient is constant and the last term in equation (15) is simple to evaluate.

7 LOWER BOUND FORMULATION WITH PORE PRESSURE

To include pore water pressure in the lower bound formulation, effective stresses are used in the yield constraints, while total stresses are employed when imposing the equilibrium and stress boundary conditions. No other changes are needed.

8 ADAPTIVE MESH REFINEMENT WITH PORE PRESSURES

To minimise the error in both the pore pressures and the bound solutions, a hybrid mesh refinement strategy is employed [1]. This first uses a Hessian (curvature)-based error estimator [13] to predict good element sizes for the pore pressures, and then applies the bounds gap scheme (as described in Section 4) to predict good element sizes for the discrete limit analysis calculations. Where the element sizes from these two separate methods differ,

the hybrid strategy simply chooses the smallest one. A Hessian-based scheme for selecting element sizes in lower bound limit analysis can be found in [14]. Exactly the same approach is adopted here, with the 'isotropic' form of the method being implemented which omits element stretching.

9 STABILITY OF SLOPE IN A WEAK LAYER

To illustrate the performance of the discrete limit analysis formulations with pore pressures and adaptive mesh refinement, we consider an example taken from the benchmark prediction exercise documented in [15]. The problem, defined in Fig. 5, has a non-circular failure surface which propagates along the weak zone, and is a challenging test for conventional slope stability methods as well as finite element limit analysis. In order to compare the new stability solutions with those reported in [15], the following strength reduction process was used to estimate the safety factor [1]:

1. Start with a trial safety factor F_0
2. Compute the available strengths $c'_a = c'/F_0$ and $\phi'_a = \tan^{-1}(\tan\phi'/F_0)$.
3. Using the available strengths (c'_a, ϕ'_a) and the adaptive discrete limit analysis algorithm with the bounds gap error indicator, compute upper and lower bounds on the unit weight that can be supported by the slope $(\gamma_{LB}, \gamma_{UB})$. Then compute the mean of the these bounds according to $\overline{\gamma} = (\gamma_{UB} + \gamma_{LB})/2$ and the gravity multiplier $m_0 = \overline{\gamma}/\gamma$, where γ is the actual unit weight.
4. If $m_0 < 1$ set $\Delta F = -\delta$, else set $\Delta F = \delta$.
5. Compute $F_1 = F_0 + \Delta F$
6. Update the available strengths according to $c'_a = c'/F_1$ and $\phi'_a = \tan^{-1}(\tan\phi'/F_1)$.
7. Using the available strengths (c'_a, ϕ'_a), find new bounds on the unit weight $(\gamma_{LB}, \gamma_{UB})$. Then compute $\overline{\gamma} = (\gamma_{UB} + \gamma_{LB})/2$ and the multiplier $m_1 = \overline{\gamma}/\gamma$.
8. If $(m_1 - 1)(m_0 - 1) > 0$, then set $m_0 = m_1$ and $F_0 = F_1$ and go to 5.
9. Linearly interpolate the factor of safety using $F = F_0 + (F_1 - F_0)(m_0 - 1)/(m_0 - m_1)$.

In step 4, $\delta \in [0.01, 0.1]$ is a constant that defines the increment in the search for the critical safety factor. The strength reduction process starts by assuming a trial estimate of the safety factor and continues with a simple marching scheme until a value is found which gives a gravity multiplier on the unit weight, *m*, of unity. Instead of taking the average of the bounds on γ to compute *m* in steps 3 and 7, it is possible to use the actual lower or upper bounds, and hence compute an upper or lower bound on the safety factor *F*. This feature may be useful for difficult problems, but it is often unnecessary due to the very tight bounds that are generated by the discrete limit analysis methods.

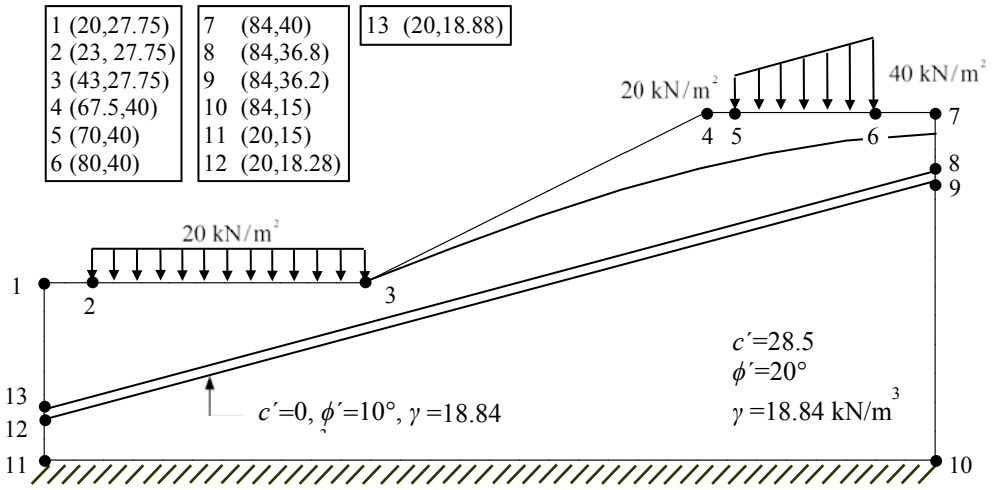

Figure 5: Slope with weak layer and pore pressure

Fig 6 shows the progress of the strength reduction process described above. Starting with an initial estimate of the safety factor of F_0=0.80 and employing a step size of δ=0.01, the algorithm gives the safety factor of F=0.822 after four iterations. This analysis, which used a maximum of 4,000 elements, required a total of about 30 seconds of CPU time on a standard desktop machine. In the vicinity of the final solution, the upper and lower bounds bracket the computed safety factor to within ±2.9%. If desired, more accurate solutions could be obtained by using more elements.

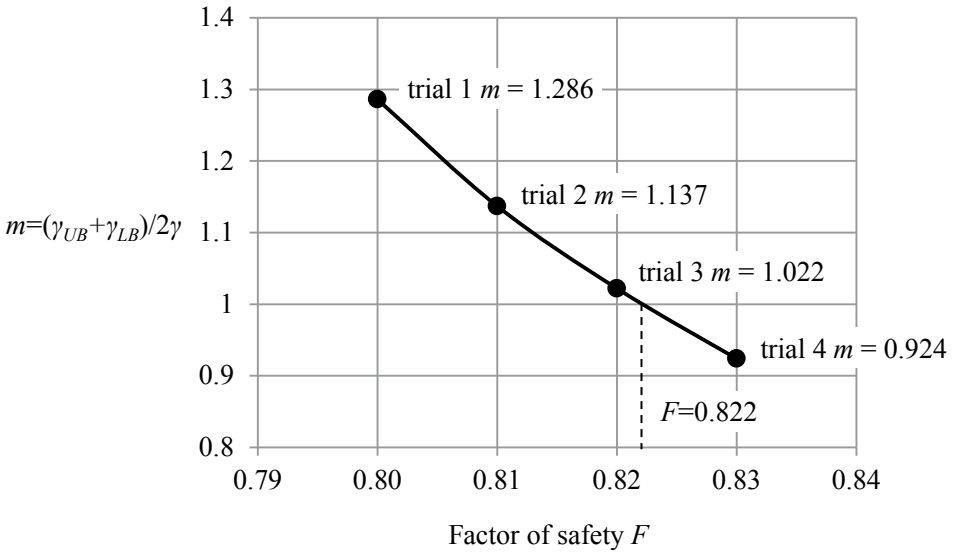

Figure 6: Strength reduction process

Fig. 7 shows the optimised mesh at the completion of the strength reduction process. This indicates that the bounds gap error measure has concentrated elements along the failure surface while, simultaneously, the Hessian-based error estimator has clustered elements around the phreatic surface. The corresponding plots of the plastic multipliers (strains) and

velocity vectors, shown in Figs 8 and 9 respectively, confirm that the mode of failure is dominated by intense shear deformation in the weak layer of cohesionless material. In addition, wedge-type mechanisms occur at the toe of the slope and behind its crest.

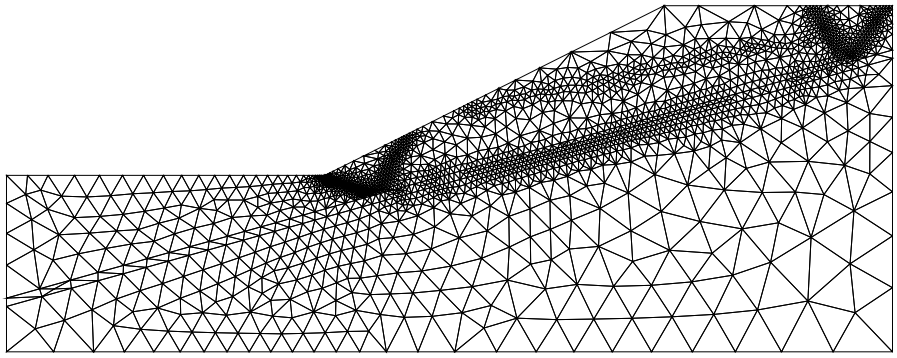

Figure 7: Optimised mesh

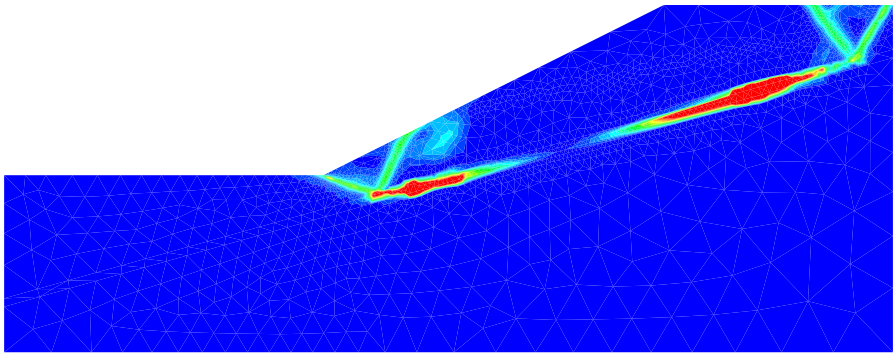

Figure 8: Plastic multiplier (strain) contours at collapse

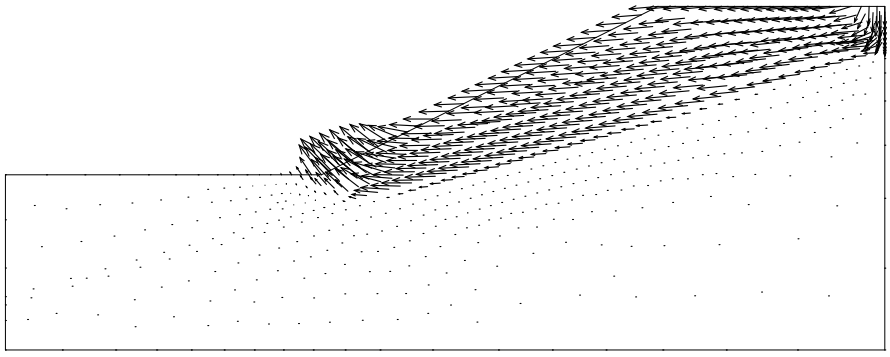

Figure 9: Velocity vectors at collapse

Fig. 10 compares the factors of safety computed from discrete limit analysis and a variety of conventional limit equilibrium methods. The latter, taken from [15], indicate a significant scatter in the estimated safety factor, even for analyses with the same technique. These variations reflect the fact that locating the critical limit-equilibrium failure surface is a

difficult unconstrained optimisation problem. Indeed, highly sophisticated search strategies are needed to obtain a reliable solution, especially if the failure surface is permitted to be non-circular. The solutions from the discrete limit analysis method, on the other hand, are guaranteed to give the best possible bounds for a specified mesh, since the governing constrained optimisation problem is convex (provided the yield surface is convex). Different limit equilibrium procedures make different assumptions in order to obtain a solution, some of which are physically more justified than others [16]. Although the Morgenstern-Price [17], Spencer [18] and Sarma [19] procedures satisfy both force and moment equilibrium for each slice, and may be viewed as 'complete equilibrium' techniques, they also give results with considerable scatter. The simplified Bishop method over-estimates the safety factor since it is better suited to cases where the failure surface can be approximated by a circle. In the study described in [15], the best estimate of the safety factor was taken to be F=0.78, which is 5% below the limit analysis predictions.

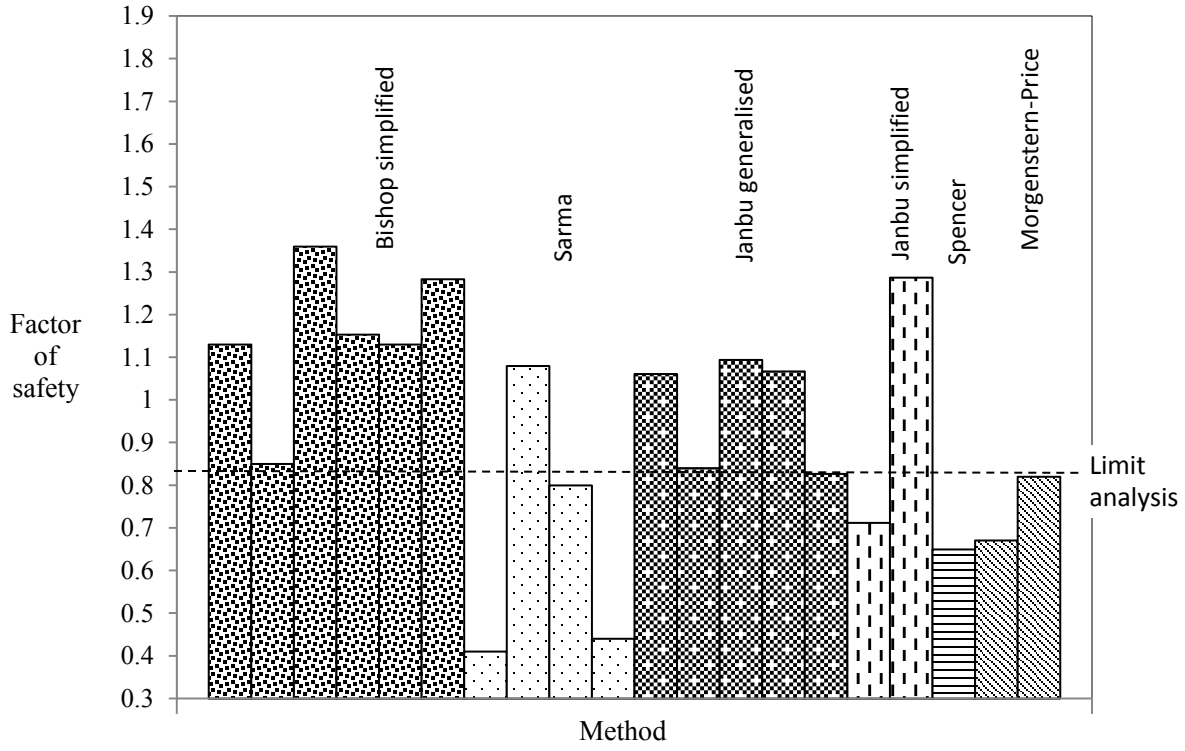

Figure 9: Comparison of safety factors

10 CONCLUSIONS

An adaptive formulation for incorporating pore pressures in discrete limit analysis has been described. The method can model the effects of both confined and unconfined seepage flow, and is a powerful new tool for practical stability analysis in geotechnical engineering.

11 REFERENCES

[1] Sloan, S.W. Geotechnical Stability Analysis. *Géotechnique*, In press (2013, 51st Rankine Lecture).

[2] Ciria, H., Peraire, J. and Bonet, J. Mesh adaptive computation of upper and lower bounds in limit analysis. *International Journal for Numerical Methods in Engineering* (2008) **75**(8):899–944.

[3] Muñoz, J.J., Bonet, J., Huerta, A. and Peraire, J. Upper and lower bounds in limit analysis: Adaptive meshing strategies and discontinuous loading, *International Journal for Numerical Methods in Engineering* (2009) **77**(4):471-501.

[4] Drucker, D.C., Greenberg W. and Prager, W. The safety factor of an elastic plastic body in plane strain. *Transactions of the ASME, Journal of Applied Mechanics* (1951) **73**:371-378.

[5] Drucker, D.C., Prager, W. and Greenberg, H.J. Extended limit design theorems for continuous media. *Quarterly Journal of Applied Mathematics* (1952) **9**(4):381–389.

[6] Lyamin, A.V. and Sloan, S.W. Upper bound limit analysis using linear finite elements and nonlinear programming. *International Journal for Numerical and Analytical Methods in Geomechanics* (2002a) **26**(2):181-216.

[7] Krabbenhøft, K., Lyamin, A.V., Hjiaj M. and Sloan, S.W. A new discontinuous upper bound limit analysis formulation. *International Journal for Numerical Methods in Engineering* (2005) **63**(7):1069-1083.

[8] Lyamin, A.V. and Sloan, S.W. Lower bound limit analysis using nonlinear programming, International Journal for Numerical Methods in Engineering (2002b) **55**:(5):573-611.

[9] Lyamin, A.V., Krabbenhøft, K., Abbo, A.J. & Sloan, S.W.. General approach for modelling discontinuities in limit analysis, *Proceedings of 11th International Conference of the International Association for Computer Methods and Advances in Geomechanics*, Torino, (2005) **1**:95-102.

[10] Ciria, H.S. *Computation of upper and lower bounds in limit state analysis using second-order cone programming and mesh adaptivity*. Ph.D. Thesis, Department of Aeronautics and Astronautics, MIT, USA, (2004).

[11] Makrodimopoulos, A. and Martin, C.M. Lower bound limit analysis of cohesive-frictional materials using second-order cone programming. *International Journal for Numerical Methods in Engineering* (2006) **66**(4):604–634.

[12] Ciria, H., Peraire, J. and Bonet, J. Mesh adaptive computation of upper and lower bounds in limit analysis. *International Journal for Numerical Methods in Engineering* (2008) **75**(8):899–944.

[13] Almeida, R.C., Feijóo, R., Gleão, A.C., Padra, C. and Silva, R.S. Adaptive finite element computational fluid dynamics using an anisotropic error estimator. *Computer Methods in Applied Mechanics and Engineering* (2000) **182**(3-4):379–400.

[14] Lyamin, A.V., Sloan, S.W., Krabbenhøft, K. and Hjiaj, M. Lower bound limit analysis with adaptive remeshing. *International Journal for Numerical Methods in Engineering* (2005) **63**(14):1961-1974.

[15] Donald, I.B. and Giam, S.K. *ACADS – Soil Slope Stability Programs Review*. ACADS publication No. U255, Melbourne, Australia, (1989).

[16] Duncan, J.M. and Wright, S.G. *Soil Strength and Slope Stability*. John Wiley & Sons, Hoboken, New Jersey, (2005).

[17] Morgenstern, N.R. and Price, V.E. The analysis of the stability of general slip surfaces. *Géotechnique* (1965) **15**(1):79-93.

[18] Spencer, E.. A method of analysis of the stability of embankments assumming parallel inter-slice forces. *Géotechnique* (1967) **17**(1):11-26.

[19] Sarma, S.K. Stability analysis of embankments and slopes. *Journal of the Geotechnical Engineering Division ASCE* (1979) **105**(12), 1511-1524.